Kekulene: On-surface synthesis, orbital structure, and aromatic stabilization

Anja Haags,[†,‡,¶,@] Alexander Reichmann,[§,@] Qitang Fan,[‖,@]
Larissa Egger,[§] Hans Kirschner,[⊥] Tim Naumann,[‖] Simon Werner,[‖]
Tobias Vollgraff ,[‖] Jörg Sundermeyer,[‖] Lukas Eschmann,[#] Xiaosheng Yang,[†,‡,¶]
Dominik Brandstetter,[§] François C. Bocquet,[†,‡] Georg Koller,[§]
Alexander Gottwald,[⊥] Mathias Richter,[⊥] Michael G. Ramsey,[§]
Michael Rohlfing,[*,#] Peter Puschnig,[*,§] J. Michael Gottfried,[*,‖]
Serguei Soubatch,[*,†,‡] and F. Stefan Tautz[†,‡,¶]

†*Peter Grünberg Institut (PGI-3), Forschungszentrum Jülich, 52425 Jülich, Germany*

‡*Jülich Aachen Research Alliance (JARA), Fundamentals of Future Information Technology, 52425 Jülich, Germany*

¶*Experimentalphysik IV A, RWTH Aachen University, 52074 Aachen, Germany*

§*Institut für Physik, Karl-Franzens-Universität Graz, NAWI Graz, 8010 Graz, Austria*

‖*Fachbereich Chemie, Philipps-Universität Marburg, Hans-Meerwein-Str. 4, 35032 Marburg, Germany*

⊥*Physikalisch-Technische Bundesanstalt (PTB), 10587 Berlin, Germany*

#*Institut für Festkörpertheorie, Westfälische Wilhelms-Universität Münster, 48149 Münster, Germany*

@*Contributed equally to this work.*

E-mail: michael.rohlfing@uni-muenster.de; peter.puschnig@uni-graz.at;
michael.gottfried@chemie.uni-marburg.de; s.subach@fz-juelich.de

Abstract

We revisit the question of kekulene's aromaticity by focusing on the electronic structure of its frontier orbitals as determined by angle-resolved photoemission spectroscopy. To this end, we have developed a specially designed precursor, 1,4,7(2,7)-triphenanthrenacyclononaphane-2,5,8-triene, which allows us to prepare sufficient quantities of kekulene of high purity directly on a Cu(111) surface, as confirmed by scanning tunneling microscopy. Supported by density functional calculations, we determine the orbital structure of kekulene's highest occupied molecular orbital by photoelectron tomography. In agreement with a recent aromaticity assessment of kekulene based solely on C–C bond lengths, we conclude that the π-conjugation of kekulene is better described by the Clar model rather than a superaromatic model. Thus, by exploiting the capabilities of photoemission tomography, we shed light on the question which consequences aromaticity holds for the frontier electronic structure of a π-conjugated molecule.

Introduction

Aromaticity, a fundamental concept of organic chemistry used to explain the stabilization of cyclic conjugated π-electron systems, has been of special interest to chemists[1] ever since the cyclic structure of benzene has been proposed by Kekulé in 1865.[2] For kekulene ($C_{48}H_{24}$) — a prototypical cycloarene — a specific aromatic stabilization mechanism has been proposed, namely the π-conjugation in two concentric macrocyclic conjugation paths denoted as [18]annulene and [30]annulene.[3–13] This so-called "superaromaticity" has been debated extensively for many years.[4–9,12,14–16] In an alternative model, kekulene is thought to consist of six disjoint aromatic sextets, thus fulfilling Clar's rule[17] according to which in benzoid molecules the number of disjoint aromatic benzene rings should be maximized and the number of double bonds minimized.

Many attempts to assess kekulene's aromaticity were solely compared to the first, and until recently the only, experimental study by Staab *et al.*,[18–20] who developed a reliable syn-

thesis of kekulene with 80 % yield.[18] The authors analyzed the obtained kekulene microcrystals by mass spectrometry, infrared adsorption and electron spectroscopies, proton nuclear magnetic resonance (^{1}H-NMR), X-ray diffraction (XRD), and optically detected magnetic resonance (ODMR).[20] However, all of these experiments were hindered by the extremely low solubility of the substance. XRD revealed a substantial variation in bond lengths and ODMR results indicated a partial compartmentation of the π-system.[19] Based on ^{1}H-NMR results[18] pointing at strong coupling between inner and outer annulene paths and thus suggestive against annulenoid ring-currents, Krieger *et al.*[19] concluded that Clar's sextet model is the better representation of the bonding situation in kekulene.

The second successful synthesis of kekulene has been reported very recently by Pozo *et al.*,[21] who synthesized kekulene in solution following the protocol by Staab *et al.*[20] The authors deposited kekulene on the cold (10 K) Cu(111) surface by rapid thermal evaporation in vacuum. Partial fragmentation due to the high sublimation temperature resulted in an adsorbate consisting of mostly small and often mobile molecules, while only few molecules with the expected hexagonal shape and size of kekulene were observed. Therefore, the investigation of kekulene has only been possible with locally resolved scanning probe methods. Using high-resolution non-contact atomic force microscopy (AFM), Pozo *et al.* have studied the geometric structure of single adsorbed molecules. By analyzing the contrast in their high-resolution AFM images and comparing with corresponding simulations, they could assess the bond-resolved bond order and hence provide insight into the aromaticity, letting the authors conclude that again the Clar model provides a better description of kekulene.[21]

In contrast to Pozo *et al.*, who focused on structural properties to assess kekulene's aromaticity, in this study, we shed light directly on the electronic structure of kekulene's frontier molecular orbitals by employing angle-resolved photoemission spectroscopy (ARPES). It is important to note that for such an area-averaging experimental technique, several requirements must be fulfilled: a sufficient number of molecules must be present on the surface, byproducts should be absent, and the majority of these molecules has to be oriented in

the same way. To meet these requirements, we developed a new on-surface synthesis route enabling the formation of a complete monolayer of well-oriented kekulene molecules, which would not have been possible via vapor deposition of kekulene. Combining density functional theory (DFT) calculations with scanning tunneling microscopy (STM) and photoemission tomography (PT)[22,23] experiments, we confirm the successful synthesis of a complete ordered kekulene monolayer and investigate the orbital structure of the highest occupied molecular orbital (HOMO). We argue that it can serve as an additional indicator of the type of aromatic bonding and give insight into the aromatic stabilization mechanism of a given molecule. By exploiting the capabilities of photoemission tomography to reveal an orbital-resolved spatial electron density,[22–29] we can unambiguously confirm Clar's model for the aromaticity of kekulene.

Results

Synthesis of kekulene on Cu(111)

The synthesis of the precursor **5** for the dehydrogenative formation of kekulene on Cu(111) proceeds in a four-step reaction sequence as summarized in Figure 1a and described in detail in the Methods section. The molecular structure of **5** shown in Figure 1b was proven by X-ray crystallography, which reveals that **5** possesses a non-planar, highly twisted conformation (see the Supporting Information (SI)).

Figure 2a shows an STM image of the as-deposited precursor **5** on a Cu(111) surface. It reveals a number of asymmetric species that are attributed to intact precursor molecules. The bright protrusions in Figure 2a are assumed to represent phenanthrene moieties tilted out of the Cu(111) surface plane due to the non-planar geometry of **5**. Annealing the sample at 500 K drastically changes the structure of the molecular layer. Figure 2b reveals a long-range ordered lattice of planar and aligned hexagonal species. With their central empty pores, they clearly resemble the structure of kekulene. Note that the free molecule

belongs to the symmetry group D_{6h},[19] or, if the small alternating out-of-plane bending of the inner hydrogens is considered, D_{3d}.[21] Therefore, we infer that upon annealing **5** undergoes a cyclodehydrogenation reaction, resulting in a molecular layer of kekulene (**6**). The density of the molecular layer confirms the high reaction yield of our on-surface synthesis. Note that the formation of large monolayer islands of kekulene on Cu(111) (or indeed any other surface) has not been reported so far.

Density functional calculations

We have performed van-der-Waals corrected density functional calculations for a monolayer of kekulene on Cu(111) by employing a repeated slab approach with six Cu-layers in order to determine the most favorable adsorption structure. As detailed in the SI, we find that the most preferable adsorption configuration is characterized by the *hcp* hollow site with kekulene's zigzag-edge oriented along the $[1\bar{1}0]$ direction of Cu(111) (cf. the side and top views depicted in Figure 2c and 2d, respectively). Note that the predicted azimuthal orientation is in agreement with the STM data. The comparably large adsorption height ($\overline{h}_{\mathrm{C}} =$ 3.05 Å), a relatively small adsorption energy (123 meV per C atom), and the flat geometry (vertical distortion $\Delta h_{\mathrm{C}=}$ 0.06 Å) indicate a rather weak interaction with Cu(111). This finding explains the large mobility of molecules reported in Ref. 21 and confirmed in our own STM experiments.

We have also analyzed the internal geometric structure, i.e., the bond lengths of the relaxed adsorbed kekulene molecule as visualized by the blue color scale in Figure 2d. Moreover, we make use of the harmonic oscillator model of aromaticity (HOMA), which is a commonly applied, purely geometric measure to quantify the aromaticity of molecules.[30–33] The HOMA value H is defined as

$$H = 1 - \frac{\alpha(n)}{n} \sum_{i=1}^{n} (R_{\mathrm{opt}} - R_i)^2. \qquad (1)$$

Here, H is related to the deformation energy of an aromatic system around its structural optimum, approximated as a harmonic potential around an optimum C–C bonding distance R_{opt}. R_{opt} itself follows from the minimization of the deformation energy and represents an ideal aromatic system. The original and fundamental idea is that each pair of carbon atoms can be involved in both, a σ- and a π-bond, with $R_\sigma > R_\pi$. The actual bonding distance R_i represents a compression of R_σ and an extension of R_π. Both terms cost energy. While this energy penalty is minimized at R_{opt}, in any given molecule the R_i may deviate from R_{opt}, which is interpreted as a local de-aromatization of the molecule. The HOMA value is a sum over n de-aromatizing contributions in the relevant part of the molecule. Note that $H = 1$ signals perfect aromaticity, while smaller H values correspond to weaker aromatic stabilization. In our calculations, the normalization parameter $\alpha(n)$ is taken from Ref. 34 and R_{opt} is calculated as the average of single- and double-bond lengths of *trans*-1,3-butadiene as obtained by our DFT calculations yielding $R_{\mathrm{opt}} = 1.403\,\text{Å}$ (cf. SI for details).

We use the HOMA (red color scale and white numbers in Figure 2 d) here as a reference for our orbital-based analysis of aromaticity to be introduced later. While the HOMA is not the only yardstick of aromaticity,[11] other suggested criteria of aromaticity based on geometric, energetic, magnetic and electronic properties of molecules are found to be in good correlation with the HOMA.[11,35,36] As an advantage of the HOMA concept, the partial equalization of bond lengths in aromatic systems, which is quantified by the HOMA value, can be easily obtained from DFT calculations. In addition, not only the aromaticity of the molecule as a whole, but also the aromaticity of any cyclic conjugation path can be easily quantified, allowing, e.g., the separate description of local, peripheral and global aromaticities.[11] Here, we evaluate H for four conjugation paths of the surface-adsorbed kekulene molecule, namely for the two inequivalent sextets $H_A = 0.65$ (ring A in Figure 1a) and $H_B = 0.92$ (ring B in Figure 1a) as well as the [18]annulene and [30]annulene paths, respectively,[37,38] ($H_{[18]} = 0.77$ and $H_{[30]} = 0.80$), each of which fulfills Hückel's $4n + 2$ condition of aromaticity and is therefore a possible candidate for affecting the aromatic stabilization of kekulene.

On the one hand, the HOMA values displayed in Figure 2d seem to indicate a propensity of kekulene towards Clar's limit as already noted by others,[3,5,11,19,21] because we observe that ring B exhibits the largest HOMA ($H_B = 0.92$). On the other hand, this conclusion is not unambiguous, because with $H_{[30]} = 0.80$, the [30]annulene path appears strongly aromatic as well. Also, the HOMA quite obviously exaggerates the peripheral aromaticity of kekulene, leading to the counterintuitive result that the aromaticity of the larger [30]annulene path is predicted to be larger than the one of smaller [18]annulene path, in contradiction to the Hückel rule, according to which π-systems with $4n + 2$ electrons are more stable for smaller n. Such an overestimation of peripheral aromaticities is a well-known problem of the HOMA concept.[11] Hence, from the purely structural deliberations, the relative importance of both postulated types of aromaticity in kekulene, Clar *versus* superaromatic model, cannot be inferred. However, it is fair to state that the above findings regarding the HOMA assess the intrinsic aromaticity of kekulene, and in particular the influence of the surface on the aromaticity of the adsorbed molecule is small (see SI).

Photoemission tomography

Up to this point, we solely concentrated on the analysis of aromaticity via bond lengths. However, aromaticity is an electronic stabilization of the molecule. To assess electronic properties of the molecule-substrate complex, we consult PT that can provide a complementary measure for aromaticity as we will show now. In the experimental photoemission band map (Figure 3a), a spectral feature from a molecular state is observed at 1.6 eV below the Fermi energy, as indicated by the dashed line, only slightly above the onset of the Cu *d*-band. The comparison with the computed projected density of states (pDOS) for kekulene/Cu(111) (Figure 3b) suggests that this emission can be assigned to the HOMO of kekulene, which, in the gas phase, belongs to the e_{1g} irreducible representation and is composed of a doubly degenerate state. To confirm this assignment, we measure a momentum map of the photoemission intensity distribution at the respective constant binding energy.

Figure 3c shows clear signatures of the molecule, namely six major lobes at $k_{\|} \approx 1.6$ Å^{-1} and six interjacent minor lobes at a slightly smaller $k_{\|} \approx 1.5$ Å^{-1}. In addition, the sharper features signal emissions from the copper *sp*-bands. The experimental momentum map is in excellent agreement with the simulated momentum map for the kekulene/Cu(111) HOMO at 1.4 eV depicted in Figure 3d. A number of conclusions can be drawn from this agreement: First, it unambiguously confirms the successful on-surface synthesis of kekulene on Cu(111) resulting in large well-orientated domains. Second, the azimuthal alignment of the molecule, as already inferred from STM and DFT, is also confirmed by the photoemission data in which the sharp *sp*-band features indicate the substrate's orientation.

We now address the primary goal of our paper to demonstrate that PT, since it is directly related to the orbital structure of frontier molecular orbitals, provides substantial insights regarding the aromaticity of molecules. To this end, Figure 4 shows the experimental and various simulated HOMO momentum maps, and in particular, it compares azimuthal intensity profiles passing through the major (L1) and minor (L2) lobes of the HOMO momentum map. Panel (a) depicts the experimental intensity profile (filled symbols) and the corresponding simulation result for kekulene/Cu(111) (open symbols) extracted from the momentum maps already presented in Figure 3c and 3d, respectively, which are replicated here for convenience in Figure 4d and 4e. These intensity profiles confirm the qualitative agreement between theory and experiment. The barely comparable backgrounds of experimental and theoretical data for the states in the vicinity of Cu *d*- and *sp*-bands prevent a full quantitative comparison of the intensity ratio between major and minor lobes.

In order to investigate how modifications in the geometry and/or electronic structure of kekulene are reflected in momentum maps of the HOMO emission, we next simulate momentum maps for the two idealized and extreme cases of the Clar and the superaromatic models of isolated kekulene, respectively. For the Clar model, we set $R_{\text{sextet}} = R_{\text{opt}}$, thus requiring maximal aromaticity of these sextets ($H_B = 1$). Contrary, for the superaromatic model we stipulate that all bonds in the annulene paths are identical, with $R_{[18]} = R_{[30]} =$

$R_{\mathrm{opt}} = 1.403$ Å to constrain that $H_{[18]} = H_{[30]} = 1$. Using these fixed geometries and neglecting the presence of the substrate, we employ DFT (for details see the SI) to compute the orbital structure of the HOMO and the corresponding momentum maps for these two model geometries. Figure 4b displays the intensity profiles of these idealized Clar (full symbols) and superaromatic (open symbols) geometries, respectively. As is evident also from the corresponding momentum maps shown in Figure 4f and 4g, respectively, the overall symmetry and appearance of the momentum maps as well as the fact that the intensity of lobe L1 is considerably larger than that of lobe L2 are preserved in both model calculations. On the one hand, this can be taken as another indication that the interaction of kekulene with Cu(111) is rather weak and therefore neglecting the substrate completely when discussing the electronic structure of kekulene seems a reasonable approach. On the other hand, and more importantly, when changing from the Clar to the superaromatic geometry, we notice only moderate changes in the orbital structure of the HOMO observed as an $\approx 10\%$ increase in the intensity of the minor lobe L2. From our DFT calculations, it thus becomes evident that changing the geometry of the molecular backbone (bond lengths) from Clar-type to superaromatic-type does not effect the electronic system profoundly. In general, this means that small variations in the geometric structure of a gapped system will not change the nodal structure of the wave-function.

Therefore, in order to impose the superaromatic stabilization by the annulene conjugation paths, we approximated the π-electron system of kekulene with a simple Hückel model.[39] This approach provides a way to tune the coupling between the inner [18]annulene path and the outer [30]annulene path by adjusting the hopping parameter t for corresponding bonds connecting them (see SI for details). In particular, a value of $t = -3.5$ eV leads to roughly the DFT result for free kekulene, as evidenced by the HOMO momentum map depicted in Figure 4h and the corresponding azimuthal intensity profile shown in Figure 4c (full symbols). If the coupling between the annulenes is completely suppressed ($t = 0$ eV), the doubly degenerate HOMO is now concentrated exclusively around the outer [30]annulene

path (as shown in the SI) and could indeed be termed "superaromatic" from an electronic structure point of view. As can be seen from Figure 4i, the corresponding momentum map is also markedly different. The formerly minor lobe L2 is almost doubled in intensity and becomes the brightest feature. Also, there are six additional lobes at larger $k_{\parallel} \approx 2.1$ Å^{-1} which are a result of the confinement of the electrons to only the outer annulene path leading to a larger spread in momentum space. None of these signatures are observed in the experimental momentum map of the HOMO (compare Figure 4d or 3c). Thus, we conclude that photoemission tomography indeed excludes a superaromatic state. Instead, all PT evidences point towards the Clar model also from an electronic structure perspective. The effect of the inter-annulene coupling on the orbital structure of the frontier orbitals HOMO and HOMO-1 both in real and in momentum space is illustrated in the SI.

Discussion and Conclusions

It remains to be clarified how exactly the orbital structure of the HOMO, as accessible via photoemission tomography, alone may serve as a sufficient measure for the aromaticity of kekulene, apparently not requiring the consideration of all π-electrons, i.e., including those in deeper-lying orbitals. To approach this question, we employ the Hückel model with $t = -3.5$ eV and analyze the orbital structures of the doubly degenerate HOMO of kekulene, denoted as HOMO$_a$ and HOMO$_b$ (Figure 5a and 5b). We observe that the electrons in the HOMO are neither confined to the inner nor the outer annulene path. Instead, the frontier electrons are delocalized over both annulene paths, and the pattern of this delocalization is already a portent of the Clar model, as a straightforward visual inspection of the electron distribution in HOMO$_a$ and HOMO$_b$ in Figure 5a and 5b shows: locally, the pair of kekulene HOMOs consists of benzene-like HOMOs (marked by the dashed lines in Figure 5a and 5b) which are located at exactly those carbon rings (ring B) where the Clar model predicts aromatic sextets (Figure 5c), while a pronounced double bond lobe appears at the corners

of kekulene (marked by dotted lines in Figure 5a and 5b). The Clar structure also becomes clearly apparent when computing the charge density as a sum of HOMO_a and HOMO_b electron distributions (Figure 5d) and comparing it with a chemical structure drawing of the Clar model of kekulene (Figure 5c): the six disjoint aromatic sextets characteristic for the Clar model can be recognized in the charge distribution of the HOMO, as well as the isolated double bonds at the corners. The evolution of kekulene's HOMO from the doubly degenerate HOMO and HOMO-1 of concentric but initially electronically decoupled [18]annulene and [30]annulene as the coupling is turned on, shown as a video in the SI, reveals that its Clar-like structure is in fact an immediate consequence of the inter-annulene coupling in kekulene and its effect on the frontier orbitals.

The enhanced significance of the HOMO for the aromaticity of kekulene is confirmed by considering its contribution to the π-bond order. In general, the bond order relates orbital structure to the bond lengths in a π-conjugated molecule, and thus also to structure-derived aromaticity parameters such as the HOMA. We define a bond order parameter b_{ij}, which we normalize by the number of contributing π-electrons N, for a given bond between carbon atoms labeled i and j in the following way:[40]

$$b_{ij} = \frac{2}{N} \sum_{m=1}^{N} a_i(m) a_j(m). \tag{2}$$

Here, $a_i(m)$ is the contribution of the p_z orbital at carbon atom i to the molecular orbital m, as resulting from the solution of the Hückel model. If all 24 occupied π-orbitals of kekulene are included in the summation of Eq. (2) (i.e., $m = 1$ to 24), plotting the bond order parameter against the DFT-optimized bond lengths for kekulene yields a clear and almost linear correlation (Figure 5e). This indicates that through the bond order parameter the nodal patterns of *all* occupied orbitals together determine the final bond lengths and thus also the HOMA-derived aromaticity in kekulene. For example, all occupied π-orbitals together lead to a large bond order for bond a (cf. Figure 5c), which therefore is short

(DFT-calculated value of $d_a = 1.37$ Å) and can be interpreted as having a strong double bond character, while bond e with its smaller bond order is longer (DFT-calculated value of $d_e = 1.46$ Å) and thus appears to be more of single bond character. Remarkably, however, there is also a pronounced correlation if we only include the doubly degenerate HOMO_a and HOMO_b in the summation ($m = 23$ to 24, Figure 5f). This reveals that the correct bond order pattern is already present in the occupied frontier orbital. It is therefore not surprising that the nodal patterns of the HOMO, which we measure in PT, are indicative of kekulene's aromaticity. Indeed, the shortest C–C bond (bond a) has a strong contribution of the HOMO charge density, while the longest C–C bond (bond e) does not (cf. Figure 5d). The disproportionate effect of the uppermost occupied π-orbitals to produce the final linear trend observed in Figure 5e also becomes apparent if only the lower half of the occupied π-states ($m = 1$ to 12) is included in the summation of Eq. (2), because then the trend is completely reversed (see SI). Interestingly, if the inter-annulene coupling is switched off ($t = 0$ eV), then the resulting bond order suggests all bonds to be of equal lengths, which is indeed the case if one was to optimize the structure of individual [18]annulene or individual [30]annulene paths.

In conclusion, using the example of on-surface synthesized kekulene we have demonstrated that the structure of occupied frontier orbitals is indeed a valid yardstick for the aromaticity of π-conjugated molecules. Since this orbital structure is accessible to photoemission tomography, the latter is a powerful complementary method to assess the role of aromatic stabilization in π-conjugated molecules.

Methods

The synthesis of the precursor **5** starts with commercially available 9,10-dihydrophenanthrene (**1**), which was regioselectively brominated to form 2,7-dibromo-9,10-dihydrophenanthrene (**2**) by applying a procedure of Wang *et al.*[41] using bromine in the absence of light. Compound **2** was oxidatively aromatized to the corresponding 2,7-dibromophenanthrene (**3**).

Subsequently, the latter was converted into bis-aldehyde (**4**) via Br-Li exchange at low temperature using *n*-butyl lithium and trapping the lithiated intermediate with dimethyl formamide (DMF) and aqueous workup. Aldehyde **4** was coupled in the last step to kekulene precursor **5** using a McMurry reaction protocol established for related targets by Majewski *et al.*[42] This protocol requires dropwise addition of **4** to a diluted reaction solution of low-valent titanium reagent formed *in situ* from titanium tetrachloride and zinc.

The kekulene precursor **5** could be obtained as beige crystalline solid in 35% yield next to higher oligomers of **4** via purification by column chromatography followed by recrystallization. The molecular structure and conformation of **5** was proven by X-ray crystallography (Figure 1b). X-ray diffractive single crystals of **5** were obtained by slow diffusion of *n*-pentane into a saturated solution of **5** in chloroform. Details of chemical synthesis and characterization of **5** are provided in the SI.

The preparation of kekulene/Cu(111), photoemission and STM experiments were performed in an ultra-high vacuum system with a base pressure in the 10^{-10} mbar range. Samples of Cu(111) were cleaned by repeating cycles of sputtering by Ar^+ ions (1.0 kV) and annealing (850 K). The molecular precursor **5** was deposited from a Knudsen-type effusion cell at 550 K onto the Cu(111) surface kept at room temperature. To trigger the reaction of cyclodehydrogenation resulting in kekulene, submonolayer films of **5** on Cu(111) were annealed at 500 K.

STM was performed with a STM Aarhus 150 microscope from SPECS GmbH. During measurements the samples were kept at 100 K.

ARPES and PT were conducted at the Metrology Light Source insertion device[43] beamline of the Physikalisch-Technische Bundesanstalt (PTB, Germany). *p*-polarized ultraviolet light (35 eV photon energy) was used with the angle of incidence of 40°. Photoelectrons were collected with the toroidal electron spectrometer.[44] For the experimental spectrum, band map and momentum map shown in Figure 3 the photoemission intensity in the emission angle range from 0° (sample normal) to +85° was used. Momentum maps were recorded by

rotating the sample in the azimuthal direction in 2° steps and measuring the photoemission intensity at a constant kinetic energy of the electrons. This results in the full photoelectron distribution in the (k_x, k_y) plane perpendicular to the sample normal.

Acknowledgement

Financial support from the Deutsche Forschungsgemeinschaft (DFG), through projects Po 2226/2-1, Ri 804/8-1, Go 1812/2-1, the SFB 1083 "Structure and Dynamics of Internal Interfaces" (projects A4, A12, and A13), and the Austrian Science Fund (FWF) (projects P27649-N20, P27427-N20, and I3731) is gratefully acknowledged. The computational results have been achieved using the computing facilities of the University of Graz and the Vienna Scientific Cluster (VSC3), as well as, of the John von Neumann Institute for Computing (NIC) on the GCS Supercomputer JUWELS at Jülich Supercomputing Centre (JSC). We thank Hendrik Kaser (PTB, Berlin) and John Riley (La Trobe, Australia) for experimental support.

Supporting Information Available

The following files are available free of charge.

- Supporting-Information.pdf: Experimental details, details of chemical synthesis, kekulene/Cu(111) sample preparation, STM, ARPES and PT, details of computational analysis, DFT, SHM, HOMA analysis.
- inter-annulene-coupling.mp4: video demonstrating the effect of electronic coupling between inner and outer annulene paths on the HOMO and HOMO-1 states of free kekulene.
- SWP148.pdf and swp148loesen.cif: CIF check and CIF files for kekulene precursor 1,4,7(2,7)-triphenanthrenacyclononaphane-2,5,8-triene.

References

(1) Balaban, A. T. Is Aromaticity Outmoded? Pure and Applied Chemistry **1980**, 52, 1409–1429.

(2) Kekulé, A. Sur la constitution des substances aromatique. Bulletin de la Société chimique de Paris **1865**, 3.

(3) Aihara, J.-I. On the Number of Aromatic Sextets in a Benzenoid Hydrocarbon. Bulletin of the Chemical Society of Japan **1976**, 49, 1429–1430.

(4) Cioslowski, J.; Mixon, S. T.; Edwards, W. D. Weak Bonds in the Topological Theory of Atoms in Molecules. Journal of the American Chemical Society **1991**, 113, 1083–1085.

(5) Aihara, J.-I. Is Superaromaticity a Fact or an Artifact? The Kekulene Problem. Journal of the American Chemical Society **1992**, 114, 865–868.

(6) Jiao, H.; Von Schleyer, P. R. Is kekulene really superaromatic? Angewandte Chemie International Edition in English **1996**, 35, 2383–2386.

(7) Zhou, Z. Are kekulene, coronene, and corannulene tetraanion superaromatic? Theoretical examination using hardness indices. Journal of Physical Organic Chemistry **1995**, 8, 103–107.

(8) Aihara, J.-I.; Makino, M.; Ishida, T.; Dias, J. R. Analytical study of superaromaticity in cycloarenes and related coronoid hydrocarbons. Journal of Physical Chemistry A **2013**, 117, 4688–4697.

(9) Aihara, J.-I. A simple method for estimating the superaromatic stabilization energy of a super-ring molecule. Journal of Physical Chemistry A **2008**, 112, 4382–4385.

(10) Buttrick, J. C.; King, B. T. Kekulenes, cycloarenes, and heterocycloarenes: Addressing electronic structure and aromaticity through experiments and calculations. Chemical Society Reviews **2017**, 46, 7–20.

(11) Setiawan, D.; Kraka, E.; Cremer, D. Quantitative Assessment of Aromaticity and Antiaromaticity Utilizing Vibrational Spectroscopy. Journal of Organic Chemistry **2016**, 81, 9669–9686.

(12) Paul, M. L. Localization of Aromaticity in Fused-Ring Cycloarene Systems. Prediction by an Effective Molecular Mechanics Model. Journal of Organic Chemistry **1988**, 53, 4590–4593.

(13) Allinger, N. L.; Li, F.; Yan, L.; Tai, J. C. Molecular mechanics (MM3) calculations on conjugated hydrocarbons. Journal of Computational Chemistry **1990**, 11, 868–895.

(14) Liu, C.; Ni, Y.; Lu, X.; Li, G.; Wu, J. Global Aromaticity in Macrocyclic Polyradicaloids: Hückel's Rule or Baird's Rule? Accounts of Chemical Research **2019**, 52, 2309–2321.

(15) Chen, Z.; King, R. B. Spherical aromaticity: Recent work on fullerenes, polyhedral boranes, and related structures. Chemical Reviews **2005**, 105, 3613–3642.

(16) Miyoshi, H.; Nobusue, S.; Shimizu, A.; Tobe, Y. Non-alternant non-benzenoid kekulenes: the birth of a new kekulene family. Chem. Soc. Rev. **2015**, 44, 6560–6577.

(17) Clar, E. The Aromatic Sextet; Wiley: London, New York, Syndey, Toronto, 1972; p 74.

(18) Diederich, F.; Staab, H. A. Benzenoid versus Annulenoid Aromaticity: Synthesis and Properties of Kekulene. Angewandte Chemie International Edition in English **1978**, 17, 372–374.

(19) Krieger, C.; Diederich, F.; Schweitzer, D.; Staab, H. A. Molecular Structure and Spectroscopic Properties of Kekulene. Angewandte Chemie International Edition in English **1979**, 18, 699–701.

(20) Staab, H. A.; Diederich, F.; Krieger, C.; Schweitzer, D. Molecular Structure and Spectroscopic Properties of Kekulene. Chemische Berichte **1983**, 116, 3504–3512.

(21) Pozo, I.; Majzik, Z.; Pavliček, N.; Melle-Franco, M.; Guitián, E.; Peña, D.; Gross, L.; Pérez, D. Revisiting Kekulene: Synthesis and Single-Molecule Imaging. Journal of the American Chemical Society **2019**, 141, 15488–15493.

(22) Puschnig, P.; Berkebile, S.; Fleming, A. J.; Koller, G.; Emtsev, K.; Seyller, T.; Riley, J. D.; Ambrosch-Draxl, C.; Netzer, F. P.; Ramsey, M. G. Reconstruction of molecular orbital densities from photoemission data. Science **2009**, 326, 702–706.

(23) Puschnig, P.; Reinisch, E. M.; Ules, T.; Koller, G.; Soubatch, S.; Ostler, M.; Romaner, L.; Tautz, F. S.; Ambrosch-Draxl, C.; Ramsey, M. G. Orbital tomography: Deconvoluting photoemission spectra of organic molecules. Physical Review B - Condensed Matter and Materials Physics **2011**, 84, 235427.

(24) Puschnig, P.; Ramsey, M. G. In Encyclopedia of Interfacial Chemistry: Surface Science and Electrochemistry; Wandelt, K., Ed.; Elsevier Science, 2018; pp 380–391.

(25) Lüftner, D.; Ules, T.; Reinisch, E. M.; Koller, G.; Soubatch, S.; Tautz, F. S.; Ramsey, M. G.; Puschnig, P. Imaging the wave functions of adsorbed molecules. Proceedings of the National Academy of Sciences of the United States of America **2014**, 111, 605–610.

(26) Lüftner, D.; Weiß, S.; Yang, X.; Hurdax, P.; Feyer, V.; Gottwald, A.; Koller, G.; Soubatch, S.; Puschnig, P.; Ramsey, M. G.; Tautz, F. S. Understanding the photoemission distribution of strongly interacting two-dimensional overlayers. Physical Review B **2017**, 96, 125402.

(27) Wießner, M.; Hauschild, D.; Sauer, C.; Feyer, V.; Schöll, A.; Reinert, F. Complete determination of molecular orbitals by measurement of phase symmetry and electron density. Nature Communications **2014**, 5, 4156.

(28) Weiß, S.; Lüftner, D.; Ules, T.; Reinisch, E. M.; Kaser, H.; Gottwald, A.; Richter, M.; Soubatch, S.; Koller, G.; Ramsey, M. G.; Tautz, F. S.; Puschnig, P. Exploring three-

dimensional orbital imaging with energy-dependent photoemission tomography. Nature Communications **2015**, 6, 8287.

(29) Yang, X.; Egger, L.; Hurdax, P.; Kaser, H.; Lüftner, D.; Bocquet, F. C.; Koller, G.; Gottwald, A.; Tegeder, P.; Richter, M.; Ramsey, M. G.; Puschnig, P.; Soubatch, S.; Tautz, F. S. Identifying surface reaction intermediates with photoemission tomography. Nature Communications **2019**, 10, 3189.

(30) Kruszewski, J.; Krygowski, T. M. Definition of aromaticity basing on the harmonic oscillator model. Tetrahedron Letters **1972**, 13, 3839–3842.

(31) Krygowski, T. M. Crystallographic Studies of Inter- and Intramolecular Interactions Reflected in Aromatic Character of π-Electron Systems. Journal of Chemical Information and Computer Sciences **1993**, 33, 70–78.

(32) Krygowski, T. M.; Cyrański, M. Separation of the energetic and geometric contributions to the aromaticity of π-electron carbocyclics. Tetrahedron **1996**, 52, 1713–1722.

(33) Krygowski, T. M.; Cyrański, M. Separation of the energetic and geometric contributions to the aromaticity. Part IV. A general model for the π-electron systems. Tetrahedron **1996**, 52, 10255–10264.

(34) Setiawan, D.; Kraka, E.; Cremer, D. Hidden Bond Anomalies: The Peculiar Case of the Fluorinated Amine Chalcogenides. Journal of Physical Chemistry A **2015**, 119, 9541–9556.

(35) Firme, C. L.; Galembeck, S. E.; Antunesa, O. A.; Esteves, P. M. Density, degeneracy, delocalization-based index of aromaticity (D_3BIA). Journal of the Brazilian Chemical Society **2007**, 18, 1397–1404.

(36) Araújo, D. M.; da Costa, T. F.; Firme, C. L. Validation of the recently developed aro-

maticity index D3BIA for benzenoid systems. Case study: acenes. Journal of Molecular Modeling **2015**, 21, 248.

(37) Stępień, M. An Aromatic Riddle: Decoupling Annulene Conjugation in Coronoid Macrocycles. Chem **2018**, 4, 1481–1483.

(38) Aihara, J.-I. Validity and limitations of the annulene-within-an-annulene (AWA) model for macrocyclic π-systems. RSC Advances **2014**, 4, 7256–7265.

(39) Hückel, E. Die freien Radikale der organischen Chemie. Quantentheoretische Beiträge zum Problem der aromatischen und ungesättigten Verbindungen. IV. Zeitschrift für Physik **1933**, 1931, 632–668.

(40) Coulson, C. A.; Lennard-Jones, J. E. The electronic structure of some polyenes and aromatic molecules. VII. Bonds of fractional order by the molecular orbital method. Proceedings of the Royal Society of London. Series A. Mathematical and Physical Sciences **1939**, 169, 413–428.

(41) Tian, H.; Shi, J.; Dong, S.; Yan, D.; Wang, L.; Geng, Y.; Wang, F. Novel highly stable semiconductors based on phenanthrene for organic field-effect transistors. Chemical Communications **2006**, 3498–3500.

(42) Majewski, M. A.; Hong, Y.; Lis, T.; Gregoliński, J.; Chmielewski, P. J.; Cybińska, J.; Kim, D.; Stępień, M. Octulene: A Hyperbolic Molecular Belt that Binds Chloride Anions. Angewandte Chemie - International Edition **2016**, 55, 14072–14076.

(43) Gottwald, A.; Kaser, H.; Kolbe, M. The U125 insertion device beamline at the Metrology Light Source. Journal of Synchrotron Radiation **2019**, 26, 535–542.

(44) Broekman, L.; Tadich, A.; Huwald, E.; Riley, J.; Leckey, R.; Seyller, T.; Emtsev, K.; Ley, L. First results from a second generation toroidal electron spectrometer. Journal of Electron Spectroscopy and Related Phenomena **2005**, 144-147, 1001–1004.

Graphical TOC Entry

Some journals require a graphical entry for the Table of Contents. This should be laid out "print ready" so that the sizing of the text is correct.
Inside the `tocentry` environment, the font used is Helvetica 8 pt, as required by Journal of the American Chemical Society.
The surrounding frame is 9 cm by 3.5 cm, which is the maximum permitted for Journal of the American Chemical Society graphical table of content entries. The box will not resize if the content is too big: instead it will overflow the edge of the box.
This box and the associated title will always be printed on a separate page at the end of the document.

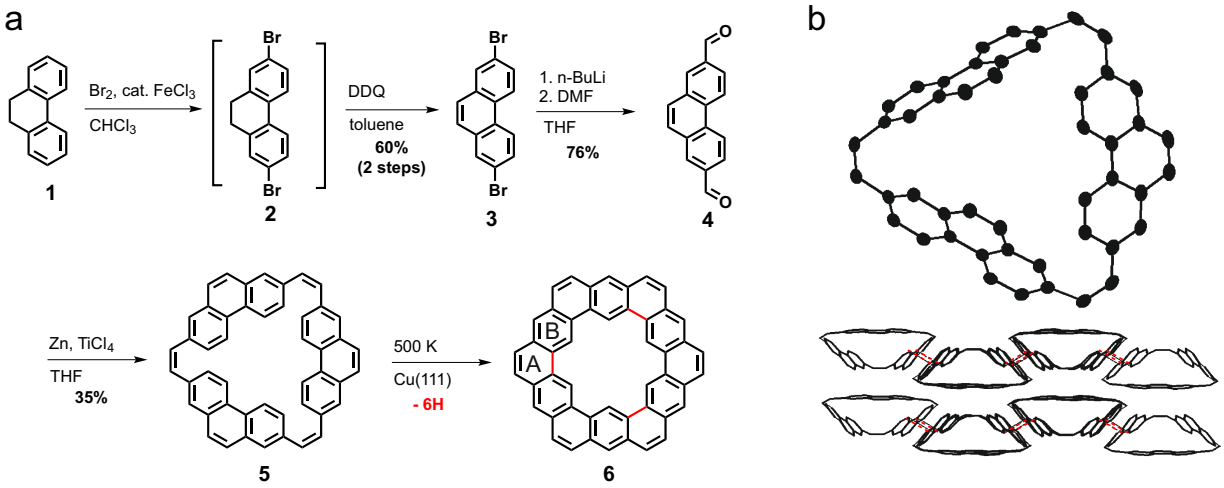

Figure 1: (a) Synthesis of kekulene precursor (**5**) by a four-step reaction sequence starting with 9,10-dihydrophenanthrene (**1**) and the on-surface reaction of **5** leading to kekulene (**6**). C–C bonds of **6** formed upon cyclodehydrogenation are marked in red. The two nonequivalent benzene rings of **6** are labeled as A and B, respectively. (b) Molecular and lattice structure obtained from single-crystal XRD analysis of **5** (thermal ellipsoids are shown at the 50% probability level and hydrogen atoms are omitted for clarity). The red dashed lines in (b) represent the shortest intermolecular C–C distance (3.34 Å).

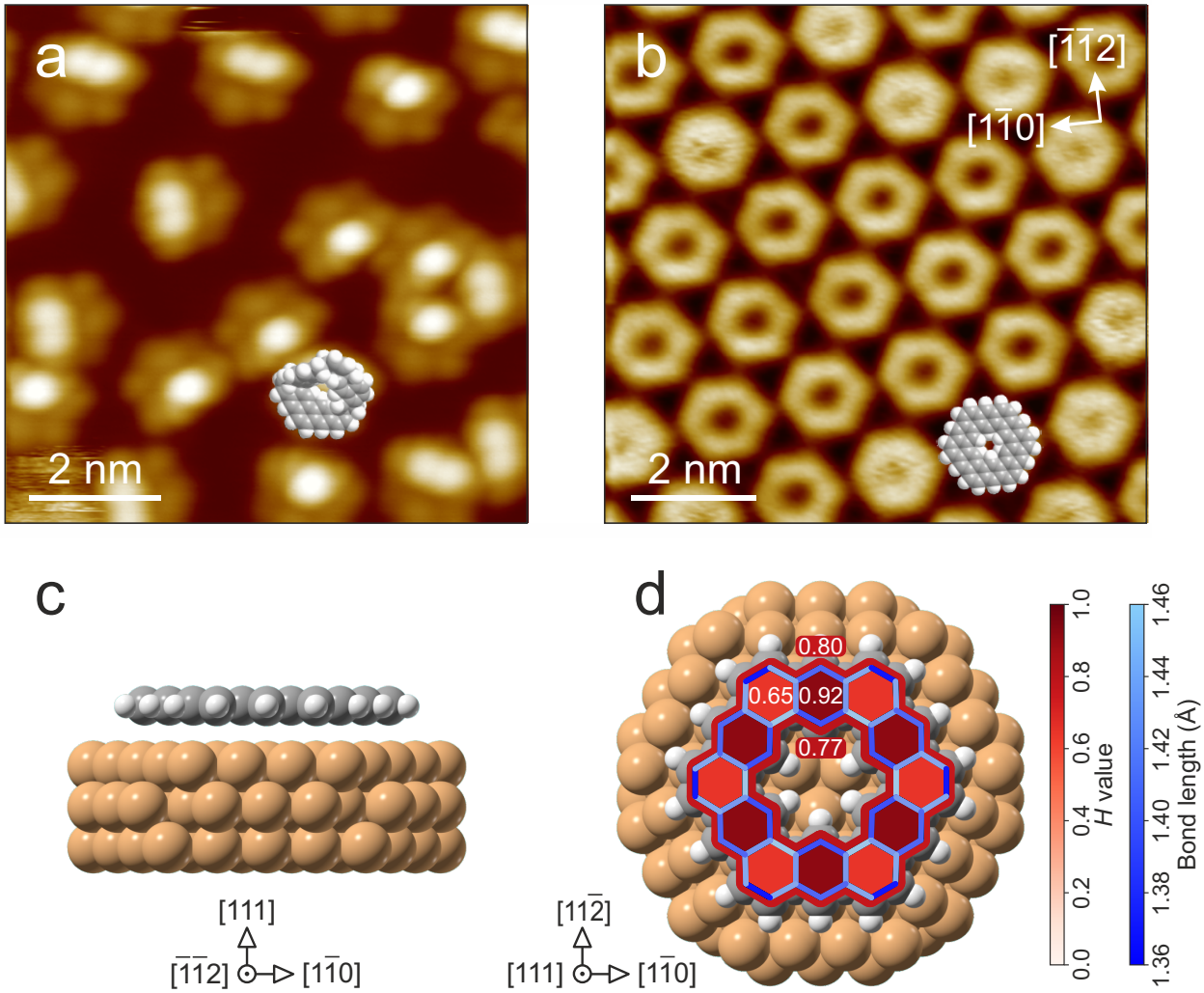

Figure 2: Structural information from STM and DFT. Panels (a) and (b) show STM micrographs of the precursor (**5**, $U = -2.8$ V, $I = 0.11$ nA) and kekulene (**6**, $U = -2.9$ V, $I = 0.26$ nA) on Cu(111), respectively. Space-filling molecular models are added to illustrate non-planar and planar molecular conformations of **5** and **6**, respectively. Panels (c) and (d) show side and top views, respectively, of the relaxed adsorption geometry of kekulene/Cu(111) as obtained by DFT. In (d), the HOMA H values as defined in the text and the bond lengths of adsorbed kekulene are color coded by red and blue colors, respectively.

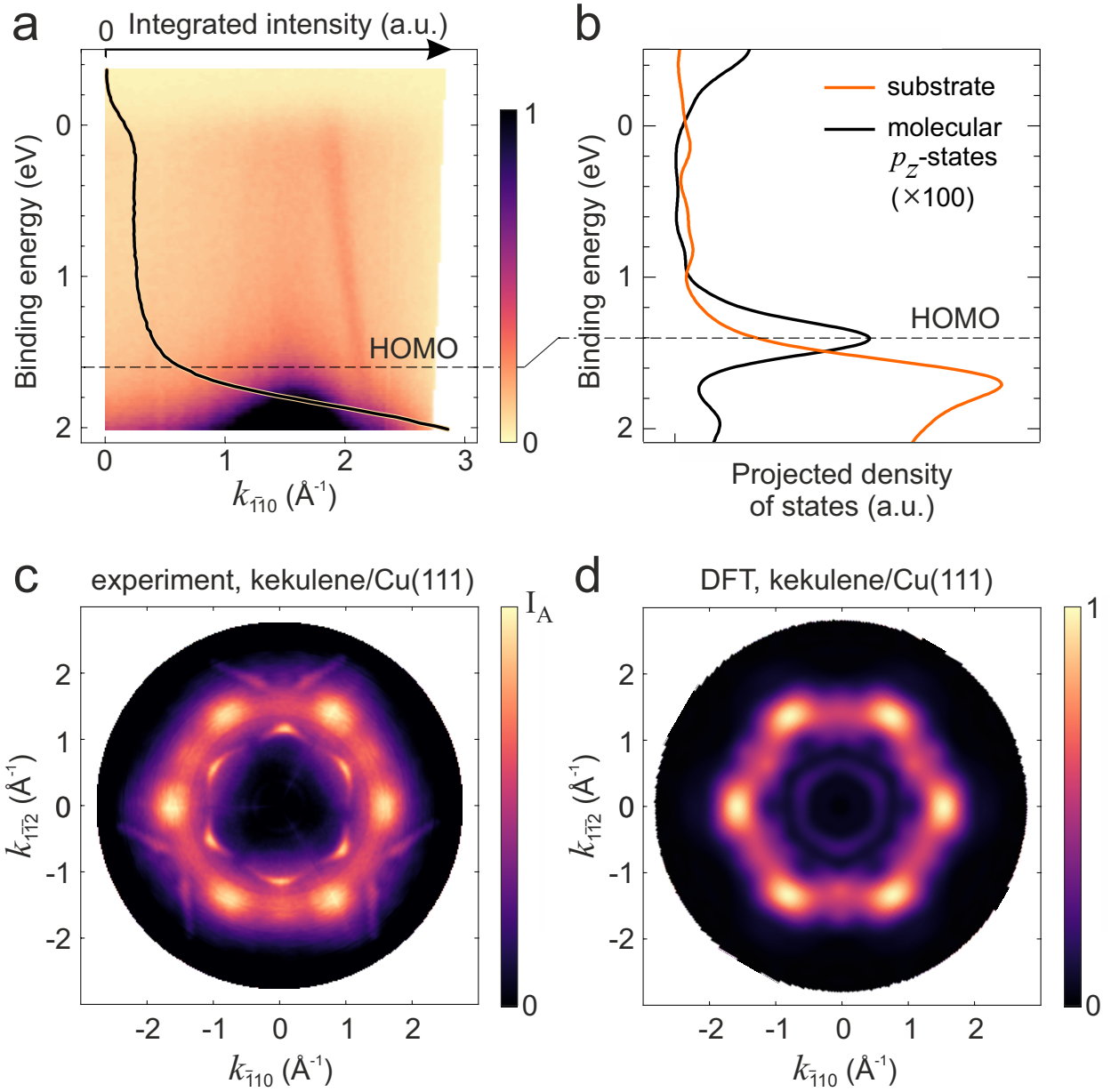

Figure 3: Angle-resolved photoemission data of kekulene/Cu(111) from experiment and theory. (a) ARPES band map along the $[1\bar{1}0]$ direction in an energy range of about 2 eV from the Fermi edge. The black line shows an angle-integrated energy distribution curve. (b) Density of states projected onto substrate (orange) and molecular p_z states (black) from DFT. Panels (c) and (d) show experimental and simulated momentum maps at the respective binding energy of the HOMO as indicated by the dashed lines in (a) and (b).

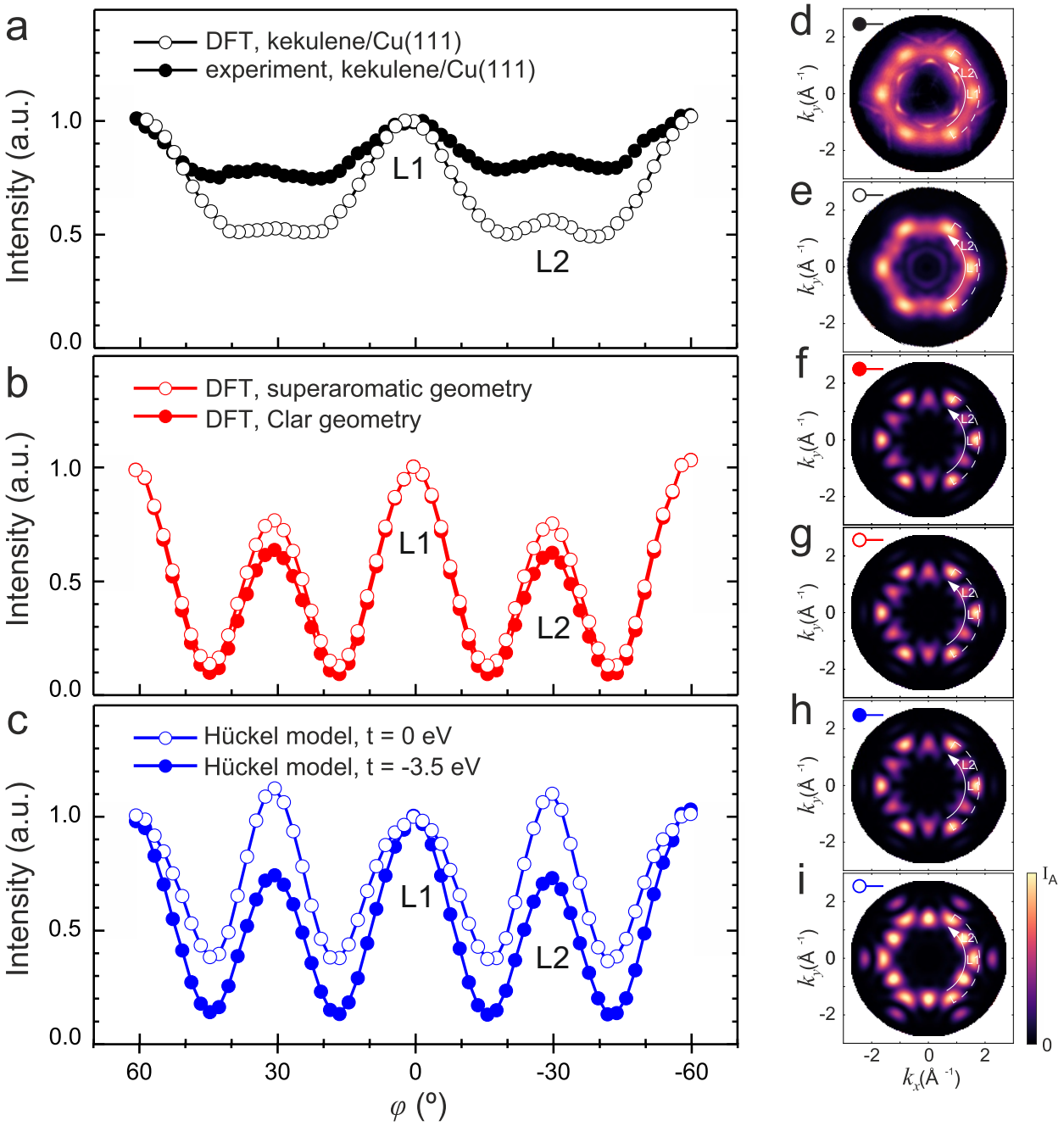

Figure 4: Comparison of experimental and simulated azimuthal ARPES intensity profiles of kekulene's HOMO. (a) Azimuthal profiles of experiment (full symbols) and simulation of kekulene/Cu(111) (open symbols) extracted from the momentum maps shown in panels (d) and (e), respectively. (b) Simulated profiles from DFT gas phase calculations of kekulene in the Clar geometry (full symbols) and superaromatic geometry (open symbols), respectively. The corresponding maps are in panels (f) and (g). (c) Simulated profiles from a Hückel model in which the coupling between inner and outer annulenes is set to $t = -3.5$ eV (full symbols) and to $t = 0$ eV (open symbols), respectively. The corresponding maps are shown in (h) and (i). Nonequivalent intensity lobes are labeled as L1 and L2. White lines in the momentum maps show the area used for intensity integration.

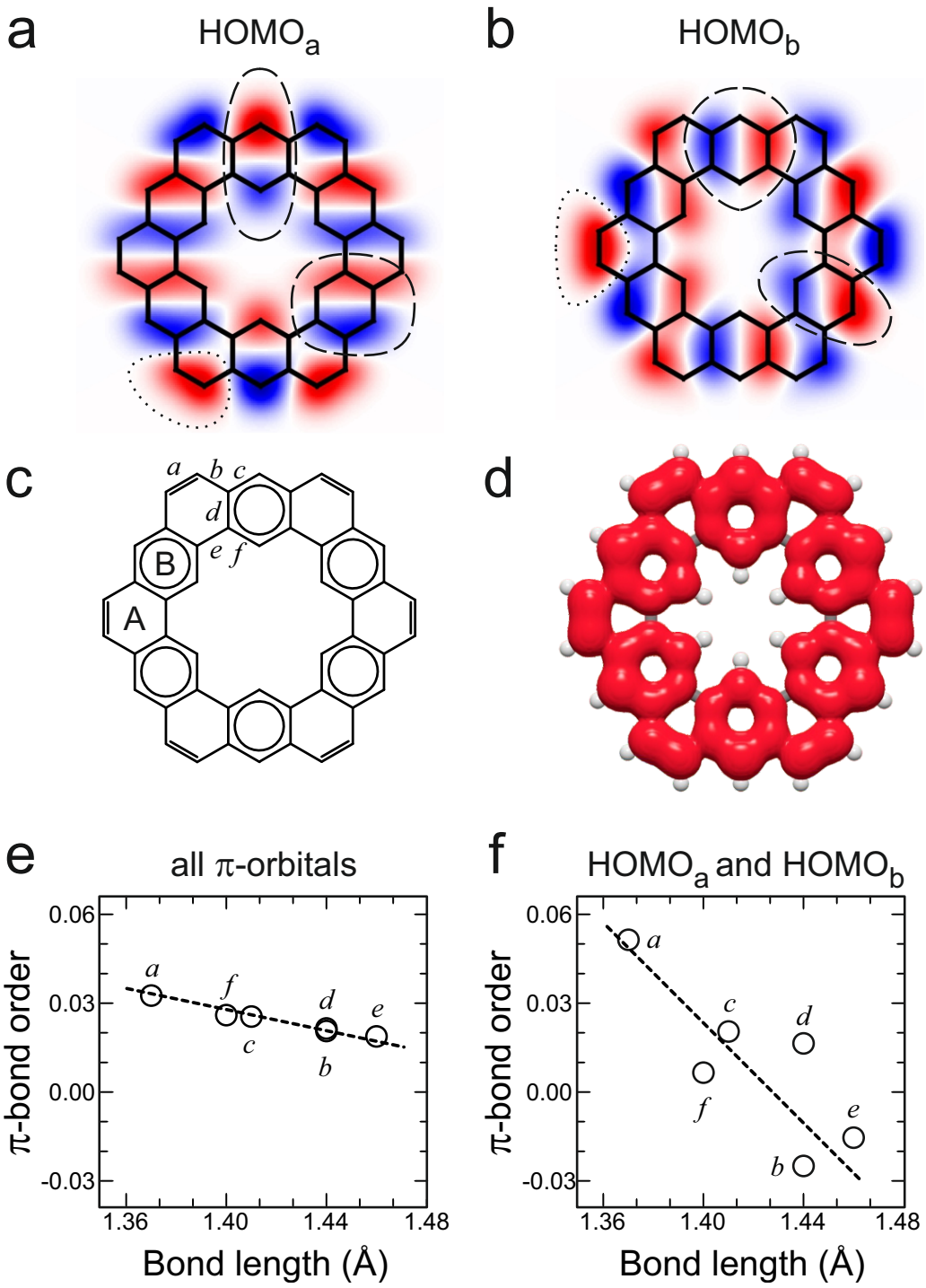

Figure 5: Kekulene's frontier electronic structure. Panels (a) and (b) show the nodal structure of the two degenerate orbitals comprising the HOMO denoted as HOMO$_a$ and HOMO$_b$, respectively. (c) Chemical structure drawing of kekulene in the Clar model with six inequivalent C–C bonds labeled as *a*, *b*, *c*, *d* and *f*. (d) Charge density distribution of the HOMO. Panels (e) and (f) depict the correlation between the C–C bond length as determined from DFT and a normalized π-bond order parameter taking into account either all 24 occupied π-orbitals or only the degenerate HOMO (m = 23 to 24) orbital. Details are described in the text.

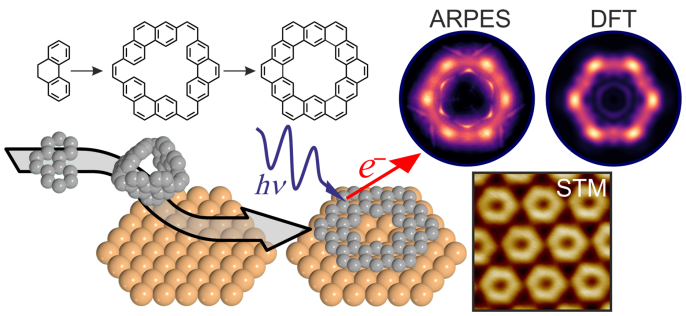

Table of Contents (TOC) graphic.